Cascade of correlated electron states in a kagome superconductor CsV_3Sb_5

He Zhao[1], Hong Li[1], Brenden R. Ortiz[2], Samuel M. L. Teicher[2], Taka Park[3], Mengxing Ye[4], Ziqiang Wang[1], Leon Balents[4], Stephen D. Wilson[2] and Ilija Zeljkovic[1,*]

[1] *Department of Physics, Boston College, Chestnut Hill, MA 02467, USA*

[2] *Materials Department and California Nanosystems Institute, University of California Santa Barbara, Santa Barbara, California 93106, USA*

[3] *Department of Physics, University of California Santa Barbara, Santa Barbara, California 93106, USA*

[4] *Kavli Institute for Theoretical Physics, University of California, Santa Barbara, Santa Barbara, California 93106, USA*

*Correspondence: ilija.zeljkovic@bc.edu

The kagome lattice of transition metal atoms provides an exciting platform to study electronic correlations in the presence of geometric frustration and nontrivial band topology[1-18], which continues to bear surprises. In this work, using spectroscopic imaging scanning tunneling microscopy, we discover a cascade of different symmetry-broken electronic states as a function of temperature in a new kagome superconductor, CsV_3Sb_5. At a temperature far above the superconducting transition $T_c \sim 2.5$ K, we reveal a tri-directional charge order with a $2a_0$ period that breaks the translation symmetry of the lattice. As the system is cooled down towards T_c, we observe a prominent V-shape spectral gap opening at the Fermi level and an additional breaking of the six-fold rotation symmetry, which persists through the superconducting transition. This rotation symmetry breaking is observed as the emergence of an additional $4a_0$ unidirectional charge order and strongly anisotropic scattering in differential conductance maps. The latter can be directly attributed to the orbital-selective renormalization of the Vanadium kagome bands. Our experiments reveal a complex landscape of electronic states that can co-exist on a kagome lattice, and provide intriguing parallels to high-T_c superconductors and twisted bilayer graphene.

Quantum solids composed of atoms arranged on a lattice of corner-sharing triangles (kagome lattice) are a fascinating playground for the exploration of novel correlated and topological electronic phenomena[1–4]. Due to their intrinsic geometric frustration, kagome systems are predicted to host to a slew of exotic electronic states[5–18], such as bond and charge ordering[7,8,10,16–18], spin liquid phases[5,15] and chiral superconductivity[9,10,17]. The majority of the experimental efforts thus far have focused on transition-metal kagome magnets, for example $Co_3Sn_2S_2$ (ref. 19–23), FeSn (ref. 24,25) and Fe_3Sn_2 (ref. 26,27), in which different forms of magnetism dominate the low-temperature electronic ground state. Electronic correlations in the absence of magnetic ordering could in principle favor the emergence of new symmetry-broken electronic states, but this has been

difficult to explore in many of the existing kagome materials due to a tendency towards magnetic ordering.

AV_3Sb_5 (A=K, Rb, Cs) is a recently discovered class of kagome metals that does not exhibit resolvable magnetic order[28,29]. This family of materials has already shown a glimpse of unusual electronic behavior in a topologically nontrivial setting, such as the large anomalous Hall response born from substantial Berry curvature[30] and a rare occurrence of superconductivity in a kagome system[29,31]. Theory indicates that the band structure of AV_3Sb_5 is characterized by a non-trivial topological invariant[29,31], which combined with emergent superconductivity, draws an interesting parallel to topological metals in the family of Fe-based high-T_c superconductors[32,33]. The large density of states due to a van Hove singularity that is located in the vicinity of the Fermi level, and quasi-1D regions of the Fermi surface[29] also provide an ideal playground for the search of elusive correlated states on a kagome lattice. While theory predicts numerous possibilities for spatial symmetry breaking of the kagome lattice electronic structure[10,17,18], their experimental realization has been challenging. In this work, using spectroscopic-imaging scanning tunneling microcopy (SI-STM), we discover a cascade of symmetry-broken phases in a kagome superconductor CsV_3Sb_5 as a function of temperature, detectable as different charge ordering states and an anisotropic quasiparticle scattering signature. These phases develop in the normal state and persist below the superconducting T_c. Our experiments demonstrate that superconductivity in CsV_3Sb_5 emerges from, and coexists with, an electronic state with an intrinsically broken rotational and translational symmetry. This could have strong implications on the superconducting order parameter in this family of kagome superconductors, where transport experiments recently suggested the possibility of unconventional pairing[34,35].

CsV_3Sb_5 is a layered superconductor (T_c~2.5 K)[29], with a hexagonal crystal structure (a=b=5.4 Å, c=9 Å) composed of V-Sb sheets stacked between complete Cs layers[28,29] (Fig. 1a,b). Each V-Sb sheet consists of a kagome network of V atoms, interlaced with a hexagonal lattice of Sb. Due to a stronger bond expected between V and Sb atoms, the material is anticipated to cleave between the V-Sb sheet and the Cs layer. Consistent with this expectation, STM topographs show two main types of atomically-ordered surface morphologies: a hexagonal lattice that we attribute to the Cs layer, and a honeycomb-like surface structure, which we ascribe to the Sb layer (Fig. 1e,f). We find that a complete Cs surface layer can be unstable, often leading to randomly distributed Cs atoms prone to clustering (Fig. 1(c,d), Fig. S1). The Sb-terminated layer is on the other hand robust, and we can routinely locate large pristine areas for imaging (Fig. S2).

In the remainder of the work, we focus on the Sb-terminated surface, located directly above the V kagome layer. Differential conductance dI/dV spectra, proportional to the local density of states, exhibit several distinct features, which are denoted by arrows in Fig. 2b. By comparison to band structure calculations, which show a good agreement with angle-resolved photoemission spectroscopy (ARPES)[29], we attribute the two spectral peaks in dI/dV spectra below the Fermi level to van Hove singularities at the M point. The local minimum between them is then likely associated with the Dirac point at K (Fig. 2a,b). To gain further insight into the electronic structure of our system, we use quasiparticle interference (QPI) imaging, rooted in the elastic scattering and interference of electrons visible as static modulations in dI/dV($\mathbf{r}$,V) maps. Aside from atomic Bragg

peaks $\mathbf{Q}^{i}_{\mathbf{Bragg}}$ (i = *a, b, c*), the Fourier transforms (FTs) of dI/dV(**r**,V) maps show an isotropic scattering vector $\mathbf{q_1}$ near the FT center (Fig. 2c, Fig. S3). By comparing its dispersion as a function of energy to theoretical band structure, we identify $\mathbf{q_1}$ as the scattering vector connecting different states on the constant energy contour of the pocket centered at Γ (Fig. 2a,c,d). The Fermi vector $\mathbf{k_f}$ ≈ 0.18 Å^{-1} obtained from our data ($\mathbf{q_1}(E = 0)=2\mathbf{k_f}$) is nearly identical to that measured by ARPES[29]. This agreement, together with the identification of spectral features in dI/dV spectra (Fig. 2a,b), demonstrates an approximate consistency between the large-scale electronic band structures measured by ARPES, STM and theory.

We proceed to investigate the system by temperature-dependent STM, starting at a high temperature well above the superconducting transition. We find that STM topographs at 60 K exhibit a 2 x 2 superstructure, which breaks the translational symmetry of the lattice (Fig. 3a). In Fourier space, this pattern gives rise to a set of wave vectors at exactly $\mathbf{q}^{i}_{\mathbf{2a0-CO}} = \frac{1}{2}\mathbf{Q}^{i}_{\mathbf{Bragg}}$ (i =*a, b, c*) (Fig. 2c, Fig. 3d-g). The vectors are extremely localized in reciprocal space (~1-2 pixels or ~ 0.006 - 0.012 Å^{-1}) and their positions do not disperse with energy (Fig. 2c, Fig. 3g, Fig. S3). Based on this, we attribute these features to a static charge order with a $2a_0$ period, propagating along all lattice directions ($2a_0$-CO). This interpretation is bolstered by X-ray diffraction measurements that detected peaks at the same wave vectors emerging below T^* = 94 K[29] and reports of charge ordering at the same wave vector in the cousin compound KV_3Sb_5 (ref. 36).

As the system is cooled down further, the electronic structure of CsV_3Sb_5 begins to display a pronounced unidirectional character. At approximately 50 K, another periodic modulation with a $4a_0$ wave length propagating along only one lattice direction emerges in STM topographs (Fig. 3b,c,e). This charge "stripe" modulation corresponds to the FT wave vector $\mathbf{q_{4a0-CO}} = 0.23\,\mathbf{Q_{Bragg}}$ (Fig. 3d,f,e,g). The small deviation between this average vector $\mathbf{q_{4a0-CO}} = 0.23\,\mathbf{Q_{Bragg}}$ and the commensurate location $0.25\,\mathbf{Q_{Bragg}}$ can be attributed to phase slips (inset in Fig. 3c). The wave vector $\mathbf{q_{4a0-CO}}$ is again non-dispersive (Fig. 3g), and thus consistent with a unidirectional charge order (1Q-CO), which has not been experimentally observed in any kagome system to-date. Upon a closer inspection of FT intensities along the same direction, we notice several faint peaks, which are equally spaced by ~$0.05\,|\mathbf{Q_{Bragg}}|$ around dominant wave vectors (Fig. S4). These cannot be explained by a linear superposition of $\mathbf{Q_{Bragg}}$, $\mathbf{q_{4a0-CO}}$ and $\mathbf{q}^{i}_{\mathbf{2a0-CO}}$, and could be a consequence of band folding, or possibly even indicative of another charge ordering state with the wave vector ~$0.05\,|\mathbf{Q_{Bragg}}|$ coupling to other peaks via satellite reflections.

In addition to static charge ordering, our SI-STM measurements reveal another intriguing aspect of the electronic structure. At low energies, FTs of dI/dV(**r**, V) maps display long parallel features, which we label as $\mathbf{q_2}$ and $\mathbf{q'_2}$ (Fig. 4b, Fig. S5). Each $\mathbf{q_2}$ and $\mathbf{q'_2}$ set of wave vectors consists of multiple parallel stripes in **q**-space. Importantly, the separation between these **q**-space stripes disperses noticeably over a narrow energy range where the feature is detected (Fig. 4c). This observation demonstrates that $\mathbf{q_2}$ and $\mathbf{q'_2}$ are related to elastic scattering between different points on the constant-energy contour (CEC) – the separation between the **q**-space features at different energies will evolve concomitantly with the change in the CEC in **k**-space. To understand the origin of scattering in more detail, we examine the morphology of the Fermi surface. The CEC

near zero energy consists of parallel quasi-1D bands along M_1-M_2 direction originating from V orbitals (inset in Fig. 4a, Supplementary Information 1). Scattering between them could naturally give rise to the unidirectional QPI observed. To visualize this, we simulate the QPI signature based on the approximate CEC, where $\mathbf{q_2}$ and $\mathbf{q'_2}$ can be beautifully reproduced (Fig. 4a, Supplementary Information 2).

Remarkably, $\mathbf{q_2}$ and $\mathbf{q'_2}$ are only observed along a single lattice vector parallel to $\mathbf{q_{4a0-CO}}$, while they are notably absent at the equivalent $\mathbf{q}$-space positions along the other two lattice directions (dashed rectangles in Fig. 4b). This provides further evidence that the electronic band structure of CsV_3Sb_5 breaks the six-fold rotational symmetry of the lattice. We rule out STM tip anisotropy effects, as the unidirectional electronic signature rotates across a domain boundary (Fig. 4f,g). As previously discussed, the C_2-symmetric signal in the FTs of dI/dV($\mathbf{r}$, V) maps originates from scattering between the states characterized by V orbitals (Fig. 4a, Fig. S11, Supplementary Section 2). This observation suggests that the rotational symmetry breaking observed is intrinsic to the V kagome layer itself. It is also important to note that it is band-specific. The QPI vector $\mathbf{q_1}$ related to the Sb pocket at Γ does not show a noticeable q-space anisotropy (Fig. 4d).

By a closer inspection of $\mathbf{q_2}$ and $\mathbf{q'_2}$ away from the Fermi energy, we find that these vectors get suppressed above 12 meV, around the same energy at which the equivalent vectors along the two other lattice directions emerge (Fig. 4d,e). This observation points towards a strong energy-dependent orbital renormalization, which is reminiscent of the orbital- and energy-dependent quasiparticle spectral weight in the electronic nematic state of Fe-based superconductors[37]. Rotation symmetry breaking could in principle be explained by either strong nematic susceptibility pinned by a small accidental strain during the sample cooldown, or an intrinsic symmetry-broken electronic phase. In strong support of the latter, we point to the following: First, symmetry-breaking QPI has been consistently observed over >100 nm square regions in multiple different crystals. Second, we can observe electronic domains in the absence of obvious structural imperfections (Fig. 4f,g, Fig. S6). Third, no $4a_0$ charge stripe order occurs at 60 K, the temperature at which the majority of the sample thermal contraction would have occurred, and yet a unidirectional modulation can be clearly seen at 50 K (Fig. 3e). Any strain-induced effects over such narrow temperature range should be negligible. Lastly, angle-dependent magnetoresistance measurements exhibit a two-fold symmetry approaching low temperature (Fig. S15b).

We hypothesize that the $2a_0$-CO arises from the nesting between the V-band van Hove points at M, giving rise to a charge order with exactly $2a_0$ wave length [10]. The formation of this $2a_0$-CO order leads to the spectral gap in dI/dV spectra with shoulders around ± 20 meV (inset in Fig. 2b, Fig. S14c,d), which we identify based on its temperature dependence (Supplementary Section 4) and recent ARPES measurements[38]. The gap opening at the Fermi level should be primarily associated with V bands, given that our QPI measurements put a bound on the gap of the Sb pocket to be 1-2 meV (Fig. S5).

A fundamental property of a single-orbital model on the kagome lattice at the van Hove filling under long range Coulomb interaction is the q=0 Pomeranchuk instability towards a rotational symmetry breaking state[17]. Our measurements uncover experimental signatures of rotation symmetry breaking on a kagome lattice, albeit with the concomitant breaking of the lattice

translation symmetry. Subleading divergences of the susceptibility predicted to occur at all wave vectors along the Γ-M directions emanating from the Γ point[17] may lead to the propensity of the electronic state to additionally break lattice translation symmetry for realistic band parameters and correlations. It is also conceivable that the translation symmetry breaking via charge ordering is related to the off van Hove filling in real materials. Such chemical potential changes or small band structure variations could possibly explain the presence (Fig. 3) or the absence[36] of the $4a_0$ charge order in different members of the AV_3Sb_5 family.

Magnetotransport experiments on CsV_3Sb_5 observed resistivity anisotropy that onsets around 50-60 K[39,40], which agrees with the onset temperature of the $4a_0$ charge order. This agreement strongly suggests that there is a bulk rotational symmetry breaking state that emerges below 50-60 K, which is either the interlayer coupled $4a_0$ charge order, or a different rotational symmetry breaking state that manifests itself on the surface as the $4a_0$ charge order. We note that a new phonon resonance also emerges around the temperature of the $4a_0$ onset[41], thus providing further evidence for the intimate relationship between the $4a_0$ charge order and the bulk of this material. Given the difference in the onset temperatures of the non-dispersive $4a_0$ 1Q-CO and the dispersive anisotropic quasiparticle scattering (Fig. S14), it may be possible that the two phenomena are associated with different parts of the same electronic bands, or different bands altogether. It remains to be understood if a vestigial order may develop from partially melting the $4a_0$ charge stripes. We note that weak quasi-1D correlations are often difficult to detect in traditional survey X-ray measurements due to the diffuse scattering signal falling below the measurement's ability to isolate it from the background. The likely presence of domain boundaries exacerbates this. Targeted scattering experiments, possibly in strained crystals to mitigate domain formation, will be necessary to determine if the $4a_0$ charge stripe order exhibits bulk correlations.

Lastly, we note that sub-Kelvin SI-STM measurements reveal that symmetry-broken states persist below the superconducting T_c (Fig. S7). The emergence of the $4a_0$ charge order, V-shape spectral gap opening in the normal state, and superconductivity presents a remarkable similarity to cuprate high-temperature superconductors[42]. At the same time, the coexistence of multiple charge orders with different wave vectors, geometries and temperature onsets in CsV_3Sb_5 adds to the complexity of the underling physics. It remains to be seen if the superconducting order parameter in CsV_3Sb_5 is unconventional, as possibly indicated by recent transport measurements[34,35]. Future experiments should address the competition of different phases by a more detailed temperature-, energy- and doping-dependent measurements, while also searching for evidence of intrinsic topological superconductivity and Majorana modes expected to arise due to the non-trivial band topology[29].

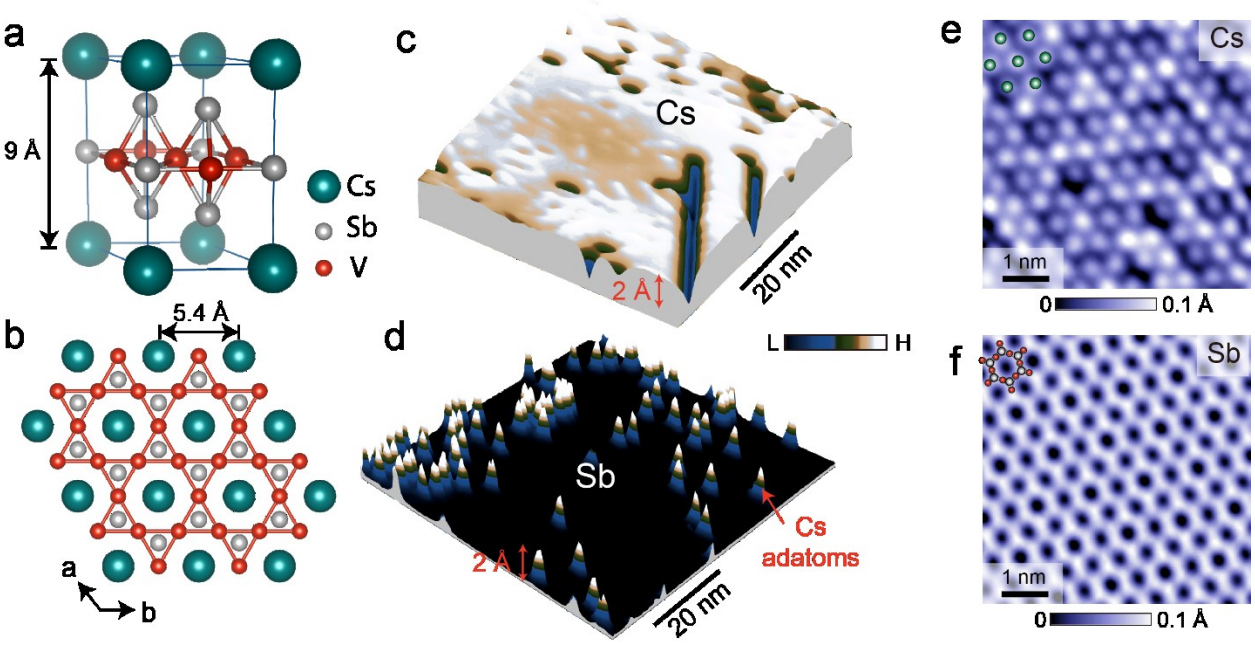

Figure 1. Surface identification. (a) 3D crystal structure of CsV_3Sb_5 viewed from the side. (b) Top-view of the crystal structure (*ab*-plane), showing the kagome lattice of the V_3Sb layer and the triangular lattice of the Cs layer. (c,d) 3D portrayal of a large-scale morphology of (c) Cs and (d) Sb layers from STM topographs. (e,f) Atomically resolved scanning tunneling microscopy (STM) topographs of (e) Cs-terminated and (f) Sb-terminated surfaces, with atom ball models superimposed. Green, gray and red spheres in (a,b,e,f) denote Cs, Sb and V atoms, respectively. STM setup condition: (c) V_{sample} = 200 mV, I_{set} = 40 pA, T = 4.5 K; (d) V_{sample} = 200 mV, I_{set} = 10 pA, T = 4.5 K, (e) V_{sample} = 20 mV, I_{set} = 200 pA, T = 4.5 K; (f) V_{sample} = 50 mV, I_{set} = 30 pA, T = 59 K;

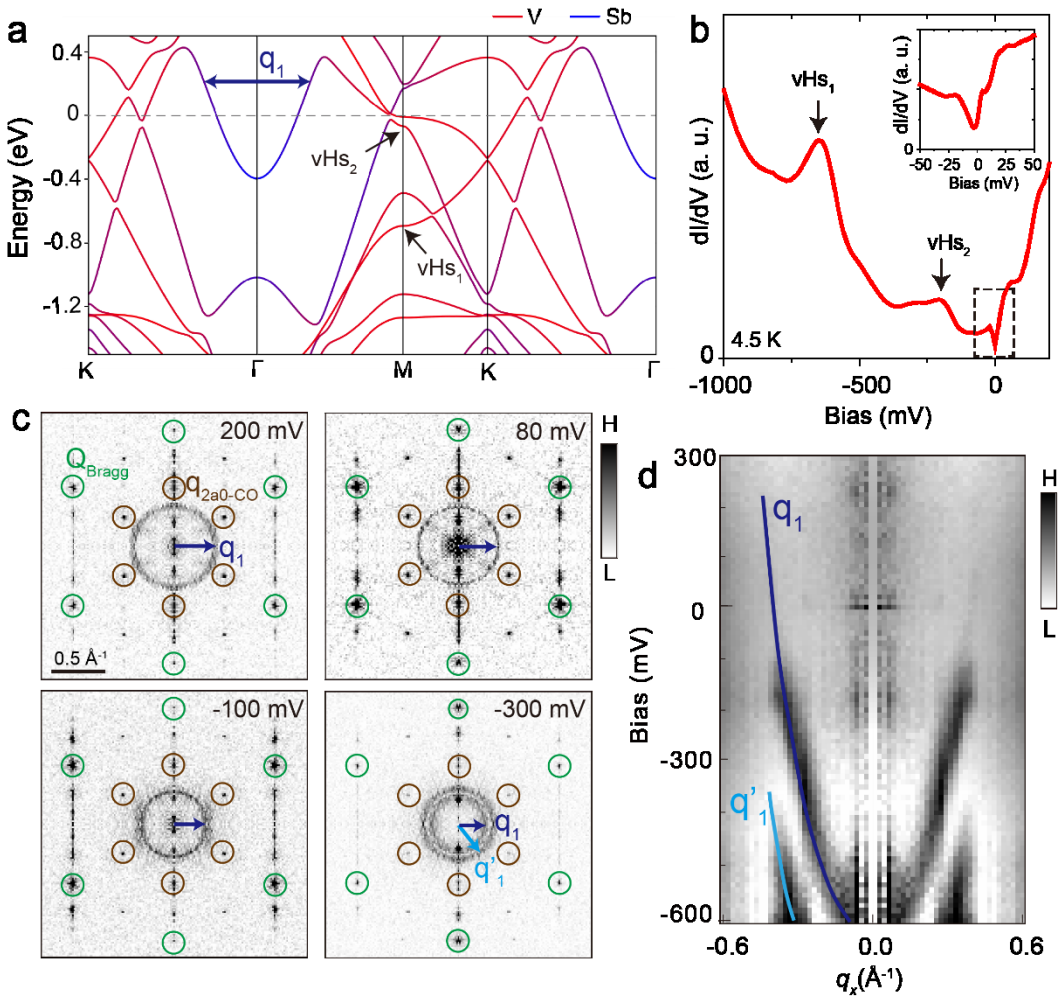

Figure 2. Large-scale electronic characterization. (a) Calculated band structure of CsV_3Sb_5, with two of the van Hove singularities ($vHs_{1,2}$) at M and one Dirac point (E_d) at K called out by arrows (Supplementary Information 1, Fig. S10). (b) Spatially averaged differential conductance (dI/dV) spectrum acquired over the Sb-terminated surface. The two peaks and the dip in the spectrum match the relative positions of the calculated $vHs_{1,2}$ and E_d, respectively, with only a small chemical potential shift. Inset in (b) displays the dI/dV spectrum over a smaller energy range close to Fermi energy (E_F). (c) Representative two-fold symmetrized Fourier transforms (FTs) of $dI/dV(\mathbf{r},V)$ maps, taken over an identical region of the Sb surface, showing prominent circle-like scattering vector $\mathbf{q_1}$. The green circles indicate the atomic Bragg peaks, while the brown circles denote the charge order $\mathbf{q_{2a0\text{-}CO}}$. (d) Radially averaged linecut in FTs of $dI/dV(\mathbf{r},V)$ maps. Dark (light) blue arrows and lines in (c,d) denote the most prominent dispersive scattering vectors $\mathbf{q_1}$ ($\mathbf{q'_1}$) in momentum-transfer space. While we cannot conclusively identify $\mathbf{q'_1}$, we hypothesize that it may be related to the same band as $\mathbf{q_1}$, and that due to a larger $\mathbf{k_z}$-dispersion at lower energies, the STM picks out dispersions related to two different, possibly extreme values of $\mathbf{k_z}$. To emphasize other features, the center pixel of FT linecut in (d) has been artificially suppressed. STM setup condition: (b) $V_{sample} = 200$ mV, $I_{set} = 500$pA, $V_{exc} = 5$ mV; inset in (b) $V_{sample} = 100$ mV, $I_{set} = 500$pA, $V_{exc} = 1$ mV; (c) $R_{tip\text{-}sample} = 0.5$ GOhms, $V_{exc} = 4$ mV; (d) $V_{sample} = 300$ mV, $I_{set} = 200$pA, $V_{exc} = 4$ mV. All data are taken at 4.5 K.

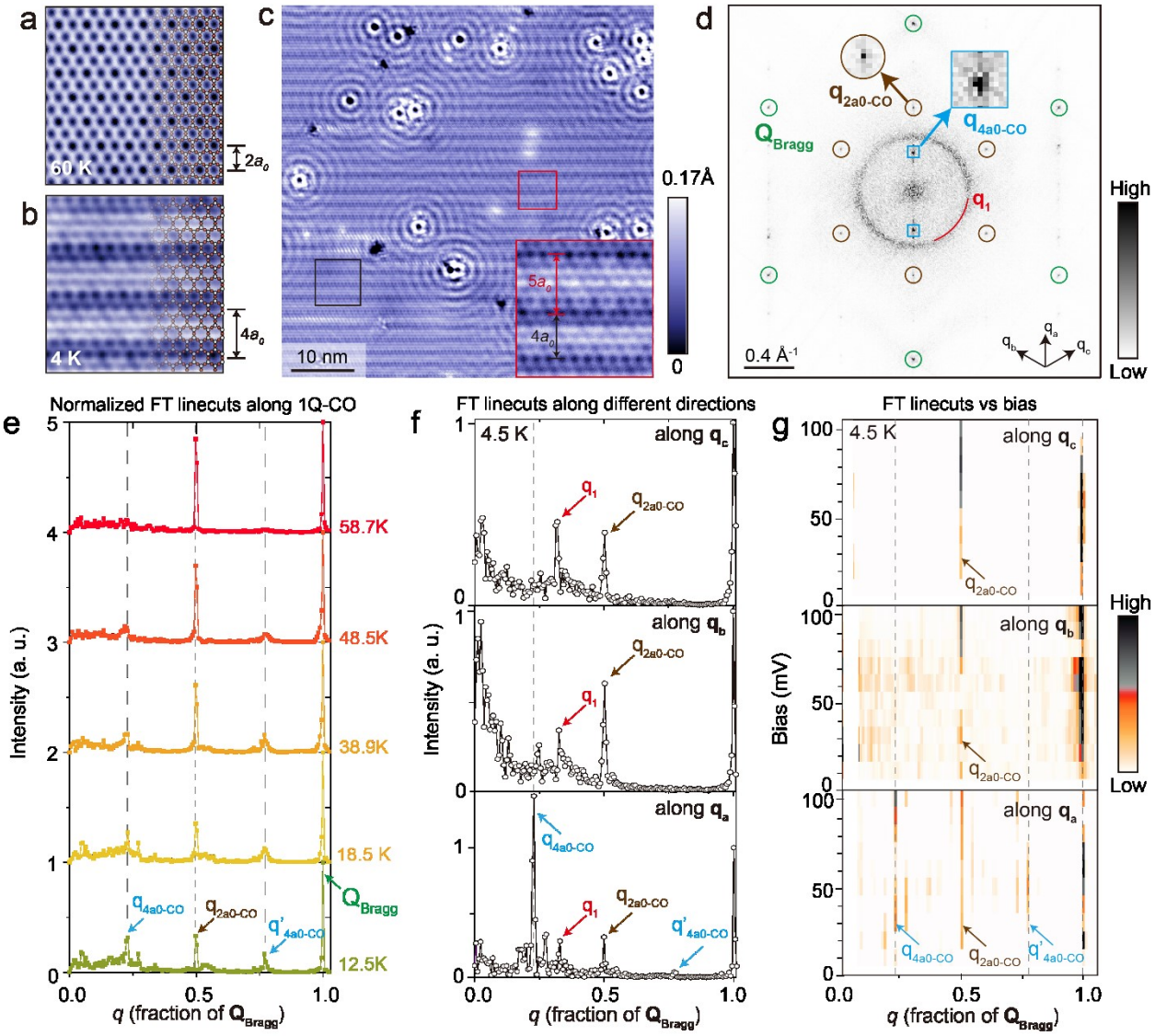

Figure 3. Charge ordering at low temperature. (a,b) Zoom-in comparison of atomically-resolved scanning tunneling microscopy (STM) topographs, taken over the Sb-terminated surface at (a) ~60 K and (b) ~4.5 K, showing different charge modulation patterns (see also Fig. S9). (c) Low-temperature STM topograph over a large region. Panel (b) is a close-up of the black squared region in the topograph in (c). Inset in (c) shows an example of a phase slip due to a $5a_0$ stripe charge modulation. The honeycomb Sb surface lattice structure is superimposed in (a,b). (d) The Fourier transform (FT) of STM topograph in (c). Green circles, brown circles and blue squares indicate the atomic Bragg peaks, $2a_0$-CO and $4a_0$-CO peaks, respectively. (e) Temperature dependent FT linecuts, along the 1Q-CO direction, all taken from data acquired over an identical region. Gray dash lines are visual guides showing a non-dispersive nature of the peaks. (f) FT linecuts along the three different lattice directions in (d). (g) FT linecuts of $L(\mathbf{r}, V)$ maps along three lattice directions at ~4.5 K as a function of bias. STM setup condition: (a) V_{sample} = 50 mV, I_{set} = 30 pA, T = 60 K; (b,c) V_{sample} = -20 mV, I_{set} = 20 pA, T = 4.5 K; (f) V_{sample} = 100 mV, I_{set} = 600 pA, V_{exc} = 4 mV, T = 4.5 K; (g) V_{sample} = -30 mV, I_{set} = 20 pA.

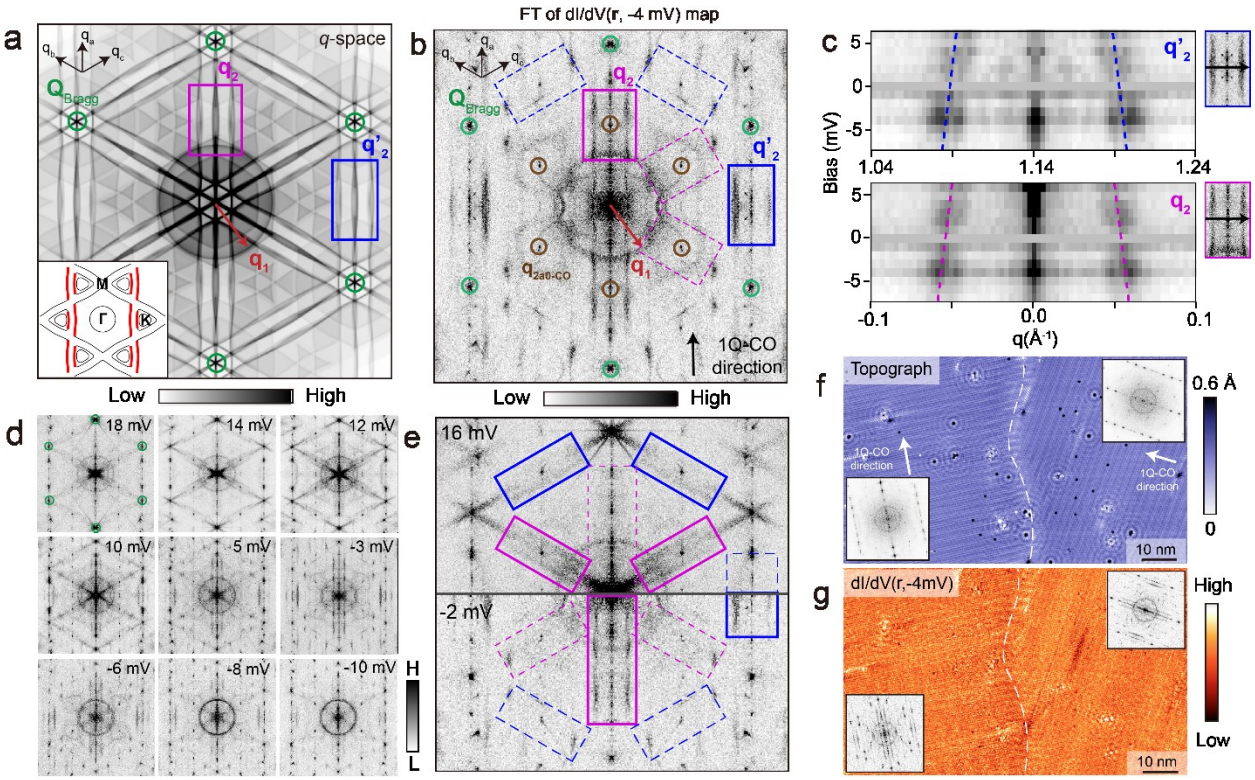

Figure 4. Visualizing rotational symmetry breaking in the quasiparticle interference (QPI) of CsV_3Sb_5. (a) Expected QPI pattern at zero energy, calculated by the autocorrelation of the approximate schematic of the Fermi surface (inset in (a), Supplementary Information 2). Red highlighted parts in the inset in (a) denote the parts of the Fermi surface that lead to the anisotropic QPI patterns (Fig. S11). (b) Two-fold symmetrized Fourier transform (FT) of differential conductance dI/dV(**r**, -4 mV) map over the Sb-terminated surface. Stripe features propagating along the $\mathbf{q}_a$ direction (solid rectangles labeled $\mathbf{q}_2$ and $\mathbf{q'}_2$), are absent in $\mathbf{q}_b$ and $\mathbf{q}_c$ lattice directions (dashed rectangles). (c) Linecuts of FTs of dI/dV(**r**, V) maps as a function of bias along the black arrows in the inset showing the dispersion of $\mathbf{q}_2$ and $\mathbf{q'}_2$. The dashed lines in (c) are visual guides. (d) Energy dependence of QPI patterns near Fermi energy. (e) Direct comparison between FTs of dI/dV(**r**, V) maps at +16 mV (top half) and -2 mV (bottom half). (f, g) STM topograph and simultaneously taken dI/dV(**r**, -4 mV) map over a region encompassing a domain boundary denoted by a dashed white curve. Insets in (f,g) on each side of the boundary show a 2-fold symmetrized FTs of the corresponding region, demonstrating the rotation of the electronic signal. For visual purposes, all FTs have been two-fold symmetrized along the 1Q-CO wave vector (see Fig. S5 for unsymmetrized FTs). STM setup condition: (b) V_{sample} = -4 mV, I_{set} = 60 pA, V_{exc} = 1 mV; (d) V_{sample} = 18 mV, I_{set} = 90 pA, V_{exc} = 1 mV; V_{sample} = 14 mV, I_{set} = 100 pA, V_{exc} = 1 mV; V_{sample} = 12 mV, I_{set} = 90 pA, V_{exc} = 1 mV; V_{sample} = 10 mV, I_{set} = 70 pA, V_{exc} = 1 mV; V_{sample} = 5 mV, I_{set} = 60 pA, V_{exc} = 1 mV; V_{sample} = -3 mV, I_{set} = 60 pA, V_{exc} = 1 mV; V_{sample} = -6 mV, I_{set} = 60 pA, V_{exc} = 1 mV; V_{sample} = -8 mV, I_{set} = 80 pA, V_{exc} = 1 mV; V_{sample} = -10 mV, I_{set} = 120 pA, V_{exc} = 1 mV, T = 4.5 K; (e) V_{sample} = 16 mV, I_{set} = 200 pA, V_{exc} = 1 mV; V_{sample} = -2 mV, I_{set} = 40 pA, V_{exc} = 1 mV; (f,g) V_{sample} = -4 mV, I_{set} = 60 pA, V_{exc} = 1 mV.

References

1. Sachdev, S. Kagome- and triangular-lattice Heisenberg antiferromagnets: Ordering from quantum fluctuations and quantum-disordered ground states with unconfined bosonic spinons. *Phys. Rev. B* **45**, 12377–12396 (1992).

2. Mazin, I. I. *et al.* Theoretical prediction of a strongly correlated Dirac metal. *Nat. Commun.* **5**, 4261 (2014).

3. Guo, H.-M. & Franz, M. Topological insulator on the kagome lattice. *Phys. Rev. B* **80**, 113102 (2009).

4. Bilitewski, T. & Moessner, R. Disordered flat bands on the kagome lattice. *Phys. Rev. B* **98**, 235109 (2018).

5. Balents, L., Fisher, M. P. A. & Girvin, S. M. Fractionalization in an easy-axis Kagome antiferromagnet. *Phys. Rev. B* **65**, 224412 (2002).

6. Neupert, T., Santos, L., Chamon, C. & Mudry, C. Fractional Quantum Hall States at Zero Magnetic Field. *Phys. Rev. Lett.* **106**, 236804 (2011).

7. Plat, X., Alet, F., Capponi, S. & Totsuka, K. Magnetization plateaus of an easy-axis kagome antiferromagnet with extended interactions. *Phys. Rev. B* **92**, 174402 (2015).

8. Wen, J., Rüegg, A., Wang, C.-C. J. & Fiete, G. A. Interaction-driven topological insulators on the kagome and the decorated honeycomb lattices. *Phys. Rev. B* **82**, 075125 (2010).

9. Yu, S.-L. & Li, J.-X. Chiral superconducting phase and chiral spin-density-wave phase in a Hubbard model on the kagome lattice. *Phys. Rev. B* **85**, 144402 (2012).

10. Kiesel, M. L., Platt, C. & Thomale, R. Unconventional Fermi Surface Instabilities in the Kagome Hubbard Model. *Phys. Rev. Lett.* **110**, 126405 (2013).

11. Sun, K., Gu, Z., Katsura, H. & Das Sarma, S. Nearly Flatbands with Nontrivial Topology. *Phys. Rev. Lett.* **106**, 236803 (2011).

12. Tang, E., Mei, J.-W. & Wen, X.-G. High-Temperature Fractional Quantum Hall States. *Phys. Rev. Lett.* **106**, 236802 (2011).

13. O'Brien, A., Pollmann, F. & Fulde, P. Strongly correlated fermions on a kagome lattice. *Phys. Rev. B* **81**, 235115 (2010).

14. Rüegg, A. & Fiete, G. A. Fractionally charged topological point defects on the kagome lattice. *Phys. Rev. B* **83**, 165118 (2011).

15. Yan, S., Huse, D. A. & White, S. R. Spin-Liquid Ground State of the S = 1/2 Kagome Heisenberg Antiferromagnet. *Science* **332**, 1173–1176 (2011).

16. Isakov, S. V., Wessel, S., Melko, R. G., Sengupta, K. & Kim, Y. B. Hard-Core Bosons on the Kagome Lattice: Valence-Bond Solids and Their Quantum Melting. *Phys. Rev. Lett.* **97**, 147202 (2006).

17. Wang, W.-S., Li, Z.-Z., Xiang, Y.-Y. & Wang, Q.-H. Competing electronic orders on

kagome lattices at van Hove filling. *Phys. Rev. B* **87**, 115135 (2013).

18. Jiang, H.-C., Devereaux, T. & Kivelson, S. A. Holon Wigner Crystal in a Lightly Doped Kagome Quantum Spin Liquid. *Phys. Rev. Lett.* **119**, 067002 (2017).

19. Wang, Q. *et al.* Large intrinsic anomalous Hall effect in half-metallic ferromagnet $Co_3Sn_2S_2$ with magnetic Weyl fermions. *Nat. Commun.* **9**, 3681 (2018).

20. Morali, N. *et al.* Fermi-arc diversity on surface terminations of the magnetic Weyl semimetal $Co_3Sn_2S_2$. *Science* **365**, 1286–1291 (2019).

21. Yin, J.-X. *et al.* Negative flat band magnetism in a spin–orbit-coupled correlated kagome magnet. *Nat. Phys.* **15**, 443–448 (2019).

22. Jiao, L. *et al.* Signatures for half-metallicity and nontrivial surface states in the kagome lattice Weyl semimetal $Co_3Sn_2S_2$. *Phys. Rev. B* **99**, 245158 (2019).

23. Liu, E. *et al.* Giant anomalous Hall effect in a ferromagnetic kagome-lattice semimetal. *Nat. Phys.* **14**, 1125–1131 (2018).

24. Lin, Z. *et al.* Dirac fermions in antiferromagnetic FeSn kagome lattices with combined space inversion and time-reversal symmetry. *Phys. Rev. B* **102**, 155103 (2020).

25. Kang, M. *et al.* Dirac fermions and flat bands in the ideal kagome metal FeSn. *Nat. Mater.* **19**, 163–169 (2020).

26. Lin, Z. *et al.* Flatbands and Emergent Ferromagnetic Ordering in Fe_3Sn_2 Kagome Lattices. *Phys. Rev. Lett.* **121**, 096401 (2018).

27. Yin, J.-X. X. *et al.* Giant and anisotropic many-body spin–orbit tunability in a strongly correlated kagome magnet. *Nature* **562**, 91–95 (2018).

28. Ortiz, B. R. *et al.* New kagome prototype materials: discovery of KV_3Sb_5,RbV_3Sb_5,and CsV_3Sb_5. *Phys. Rev. Mater.* **3**, 094407 (2019).

29. Ortiz, B. R. *et al.* CsV_3Sb_5: A Z2 Topological Kagome Metal with a Superconducting Ground State. *Phys. Rev. Lett.* **125**, 247002 (2020).

30. Yang, S.-Y. *et al.* Giant, unconventional anomalous Hall effect in the metallic frustrated magnet candidate, KV_3Sb_5. *Sci. Adv.* **6**, eabb6003 (2020).

31. Ortiz, B. R. *et al.* Superconductivity in the Z_2 kagome metal KV_3Sb_5. *Phys. Rev. Mater.* **5**, 034801 (2021).

32. Wang, D. *et al.* Evidence for Majorana bound states in an iron-based superconductor. *Science* **362**, 333–335 (2018).

33. Zhang, P. *et al.* Observation of topological superconductivity on the surface of an iron-based superconductor. *Science* **360**, 182–186 (2018).

34. Wang, Y. *et al.* Proximity-induced spin-triplet superconductivity and edge supercurrent in the topological Kagome metal, $K_{1-x}V_3Sb_5$. *ArXiv:* 2012.05898 (2020).

35. Zhao, C. C. *et al.* Nodal superconductivity and superconducting dome in the topological

Kagome metal CsV_3Sb_5. *Arxiv:* 2102.08356 (2021).

36. Jiang, Y.-X. *et al.* Unconventional chiral charge order in kagome superconductor KV_3Sb_5. *Nat. Mater.* (2021). doi:10.1038/s41563-021-01034-y

37. Kostin, A. *et al.* Imaging orbital-selective quasiparticles in the Hund's metal state of FeSe. *Nat. Mater.* **17**, 869–874 (2018).

38. Nakayama, K. *et al.* Multiple Energy Scales and Anisotropic Energy Gap in the Charge-Density-Wave Phase of Kagome Superconductor CsV_3Sb_5. *ArXiv:* 2104.08042 (2021).

39. Xiang, Y. *et al.* Twofold symmetry of c-axis resistivity in topological kagome superconductor CsV_3Sb_5 with in-plane rotating magnetic field. *ArXiv:* 2104.06909 (2021).

40. Chen, H. *et al.* Roton pair density wave and unconventional strong-coupling superconductivity in a topological kagome metal. *ArXiv:* 2103.09188 (2021).

41. Ratcliff, N., Hallett, L., Ortiz, B. R., Wilson, S. D. & Harter, J. W. Coherent phonon spectroscopy and interlayer modulation of charge density wave order in the kagome metal CsV_3Sb_5. *ArXiv:* 2104.10138 (2021).

42. Fradkin, E., Kivelson, S. A. & Tranquada, J. M. Colloquium : Theory of intertwined orders in high temperature superconductors. *Rev. Mod. Phys.* **87**, 457–482 (2015).

43. Lawler, M. J. *et al.* Intra-unit-cell electronic nematicity of the high-Tc copper-oxide pseudogap states. *Nature* **466**, 347–351 (2010).

Methods

Single crystals of CsV_3Sb_5 were grown and characterized as described in more detail in Ref. [29] (Fig. S15). We cold-cleaved and studied three different CsV_3Sb_5 crystals, all of which exhibited qualitatively the same phenomena described in the main text (Fig. S8). STM data was acquired using a customized Unisoku USM1300 microscope at varying temperatures denoted in figure captions. Spectroscopic measurements were made using a standard lock-in technique with 915 Hz frequency and bias excitation as also detailed in figure captions. STM tips used were home-made chemically-etched tungsten tips, annealed in UHV to bright orange color prior to STM experiments. To remove the effects of small piezoelectric and thermal drifts during the acquisition of data, we apply the Lawler-Fujita drift-correction algorithm [43] on all our data, which aligns the atomic Bragg peaks in STM topographs to be exactly equal in magnitude and 60 degrees apart. This process is done prior to two-fold symmetrization of Fourier transforms displayed in Figures 2 and 4, which are mirror-symmetrized around the direction of the $4a_0$ charge ordering wave vector (see Fig. S5 for more details).

Acknowledgements

I.Z. gratefully acknowledges the support from the National Science Foundation grant no. NSF-DMR-1654041 and Boston College startup. S.D.W, B.R.O, L.B, S.T, and T.P. gratefully acknowledge support via the UC Santa Barbara NSF Quantum Foundry funded via the Q-AMASE-i program under award DMR-1906325. B.R.O. also acknowledges support from the California NanoSystems Institute through the Elings Fellowship program. We acknowledge use of the shared computing facilities of the Center for Scientific Computing at UC Santa Barbara, supported by NSF CNS-1725797, and the NSF MRSEC at UC Santa Barbara, NSF DMR-1720256. S.T. has been supported by the National Science Foundation Graduate Research Fellowship Program under Grant no. DGE-1650114. Any opinions, findings, and conclusions or recommendations expressed in this material are those of the authors and do not necessarily reflect the views of the National Science Foundation. Z.W. acknowledges the support of U.S. Department of Energy, Basic Energy Sciences Grant No. DE-FG02-99ER45747.

Author Contributions

STM experiments and data analysis were performed by H.Z and H.L. B.R.O. synthesized and characterized the samples under the supervision of S.D.W. S.M.L.T. performed band structure calculations. T.P., M.Y., L.B. and Z.W. provided theoretical input on the underlying physics and the interpretation of data. H.Z., S.D.W., Z.W. and I.Z. wrote the paper, with the input from all authors. I.Z. supervised the project.

Competing Interests

The Authors declare no Competing Financial or Non-Financial Interests.

Code availability

The computer code used for data analysis is available upon request from the corresponding author.

Data Availability

The data supporting the findings of this study are available upon request from the corresponding author.

Supplementary Information is available for this paper.

Correspondence and requests for materials should be addressed to I.Z.